Article

Numerical Investigation on the Pulling Resistant Capacity of Steel Beam-Concrete Wall Joints with T-stub Connectors

He Zhao [1,2], Long-Hui Sun [1], Hong-Bing Chen [1] and Xiao-Gang Liu [1,*]

[1] Research Institute of Urbanization and Urban Safety, School of Civil and Resource Engineering, University of Science and Technology Beijing, Beijing 100083, China
[2] Key Laboratory of Civil Engineering Safety and Durability of China Education Ministry, Department of Civil Engineering, Tsinghua University, Beijing 100084, China
* Correspondence: liuxiaogang@ustb.edu.cn

Abstract: The steel frame-reinforced concrete core tube structural system is widely used in mid-rise and high-rise buildings due to its good seismic behaviour and high construction efficiency. Since the steel frame and the reinforced concrete core tube are supposed to deform synergistically under earthquake action, the steel beam-concrete wall joint (SBCW joint for short) will be subjected to a significant pull-out force. Therefore, the pulling resistant capacity of the SBCW joint is quite important for the seismic performance of the overall structure. In response to the shortages of the existing SBCW joint types, a new SBCW joint with a T-stub connector was proposed and studied. The experimental and analytical research has indicated that there are different failure modes and force mechanisms of the SBCW joint under pull-out load, and further studies are required for the pulling resistant capacity. On the basis of recent research findings, a numerical investigation on the pulling resistant capacity of the joint is conducted in this study. An elaborate 3D finite element model of the SBCW joint is proposed, and the load performance, strain and stress development, deformation characteristics and failure modes are analysed in detail. Then, a series of parametric analyses are carried out based on the finite element model, indicating that the length and the web height of the T-stub connector, the number of shear studs on the connector and the reinforcement ratio of stirrups have an obvious effect on the pulling resistant capacity. Finally, the critical value of the embedded depth of the connector, which is found to be one of the most important parameters for the failure mode and pulling resistant capacity of the joint, is determined, and design recommendations are proposed for the SBCW joints with T-stub connectors.

Keywords: SBCW joint; T-stub connector; pulling resistant capacity; numerical model; failure mode; nonlinear analysis

1. Introduction

The steel frame-reinforced concrete core tube structural system as shown in Figure 1a demonstrates high bearing capacity and good utility function, in which the core tube provides the majority of the lateral stiffness and the perimeter steel frame provides large and flexible space [1,2]. In addition, the construction of steel frames is much easier than that of reinforced concrete frames, which can greatly increase construction efficiency. Therefore, the steel frame-reinforced concrete core tube structural system is commonly used in mid-rise and high-rise buildings [3]. In this hybrid structural system, the force mechanisms and deformation patterns of the steel frame and the reinforced concrete core tube are quite different. Therefore, the steel beam-concrete wall joint (SBCW joint for short), as illustrated in Figure 1b, plays a critical role in the cooperative work of the two structural components to achieve satisfactory seismic performance of the whole structural system [4,5].
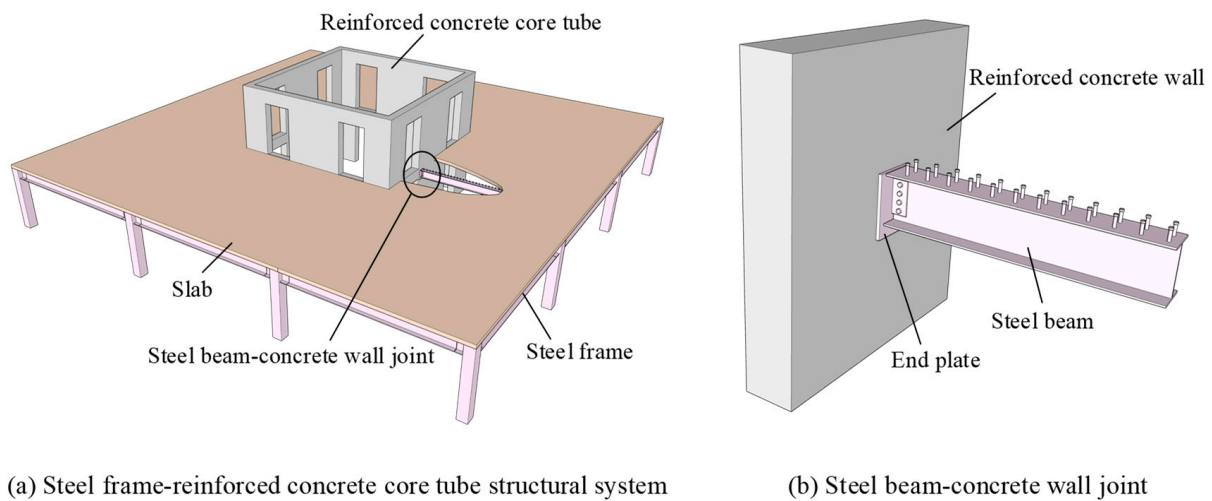
(a) Steel frame-reinforced concrete core tube structural system   (b) Steel beam-concrete wall joint

Figure 1. The SBCW joint in a steel frame-reinforced concrete core tube structural system.

Previous studies [6,7] have indicated that the connector, of which the main part is embedded in the concrete wall and one end is connected to the steel beam, is quite important to the mechanical properties and failure modes of the SBCW joints. Common types of connectors include shear studs, anchorage bars or small steel plates and H-shaped steel. The SBCW joint with shear stud connectors was first proposed and studied. In the 1980s, Hawkins et al. [8] and Roeder and Hawkins [9] carried out experiments on this type of joint under combined shear force and bending moment and developed a design procedure. Then in the early 21st century, Shahrooz et al. [10,11] investigated the mechanical behaviour of outrigger beam-wall connections with multiple headed studs under a constant shear force and cyclic axial load considering the effects of cracking, damage and yielding of reinforcements. The force mechanism of the SBCW joint with anchorage bars or steel plates is similar to that of the first joint type. The shear and flexural behaviour of the second type was investigated by monotonic and cyclic tests and compared with that of the first type [6]. The experimental results indicated that the failure of the second type was determined by the steel connectors while the first type demonstrated the concrete split failure mode, which was more brittle. Li et al. [12] studied the seismic behaviour of the SBCW joint with anchorage bars, and the slippage of anchorage bars was observed in the tests. The third type with H-shaped steel connectors has higher strength and stiffness than the other two types based on the experimental and numerical investigations [13].

Although various types of SBCW joints have been proposed and investigated, there are shortcomings for the existing types. The joints with shear stud connectors are prone to brittle concrete failure. The pulling resistant capacity of the joints with anchorage bars or small steel plates is relatively low, which makes is difficult for them to bear the significant axial force under earthquake action [14–16]. The H-shaped steel connector requires large space in the concrete wall, which would lead to difficulties in the arrangement of wall reinforcements. In addition, previous research mainly focused on the shear and flexural performance of the SBCW joints and there were few specific studies on the pull-out behaviour. Therefore, an SBCW joint with a T-stub steel connector as shown in Figure 2 was proposed by Zhao et al. [17] to improve the pulling resistant capacity and facilitate construction. Six full-scale specimens were tested and theoretical models were proposed for concrete breakout failure and steel web yield failure, respectively. It was indicated that the parameters of the T-stub connector and wall reinforcements had influences on the pull-out behaviour of the joint. However, the impact mechanism has not been studied clearly due to the limited number of tests. Therefore, substantial finite element analysis of the pulling resistant capacity needs to be carried out to determine the critical design parameters of SBCW joints with T-stub connectors.
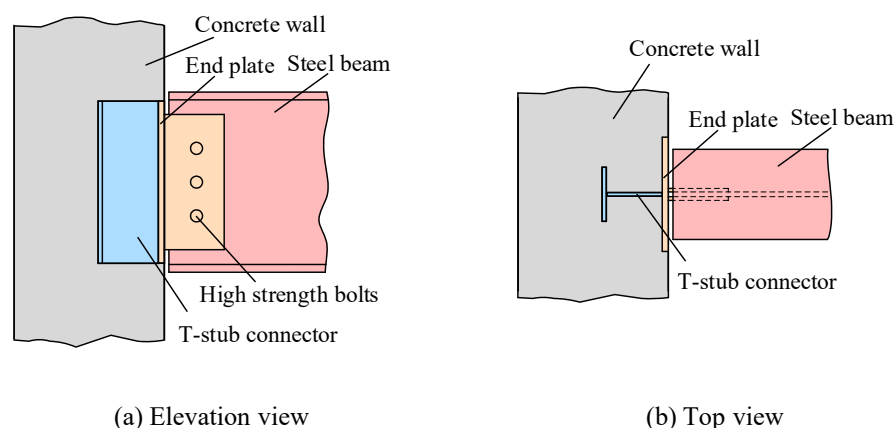
Figure 2. The SBCW joint with a T-stub steel connector.

2. Aim and Scope

In this study, the pull-out behaviour of SBCW joints with T-stub connectors is investigated in detail using numerical techniques. A finite element model of the joint is established by general commercial FE package MSC.MARC Version 2012 [18]. It is well known that the modelling of punching shear behaviour of concrete is a major challenge in numerical simulation [19,20]. The established finite element model can reasonably consider the failure of concrete by adopting a modified shear retention factor. The accuracy of the finite element model is verified by comparing the test and numerical results. Then, the effects of different design parameters, including the length of the T-stub connector, the flange width of the T-stub connector, the number of shear studs on the web of the T-stub connector, the web height of the T-stub connector and the reinforcement ratio of stirrups, on the pull-out performance of the joint are investigated based on the numerical model. Parametric analyses indicate that the embedded depth of the connector is the most important parameter for the failure mode. Finally, the critical value of the embedded depth is discussed on the basis of the numerical model and theoretical model. The research findings in this paper can reveal the force mechanism of SBCW joints with T-stub connectors under pull-out load and provide references for the design of the joints.

3. Numerical Modelling

3.1. Model Setup

The finite element models were built to simulate the pull-out behaviour of the SBCW joints with T-stub connectors. Figure 3 illustrates the detailed geometric information of the components of the joint, including the steel components and the reinforced concrete wall. The investigated parameters, i.e., the length of the T-stub connector l_c, the flange width of the T-stub connector w_f, the web height of the T-stub connector h_w, the number of shear studs on the web of the T-stub connector n_s and the reinforcement ratio of stirrups r_s, which is calculated as the ratio of cross-sectional area of stirrups to the area of the concrete wall surface perpendicular to the stirrups, are marked in red in Figure 3. These parameters for the six test specimens in [17] are listed in Table 1. Due to the limited number of specimens, the parameters l_c and w_f, which are considered critical parameters, were designed the same for all the tests. The setup of the tests is shown in Figure 4. The two ends of the concrete wall were simply supported, and a loading frame bolted to the steel beam was utilised to convert the pressure load from the loading jack into the tensile load applied to the joint.
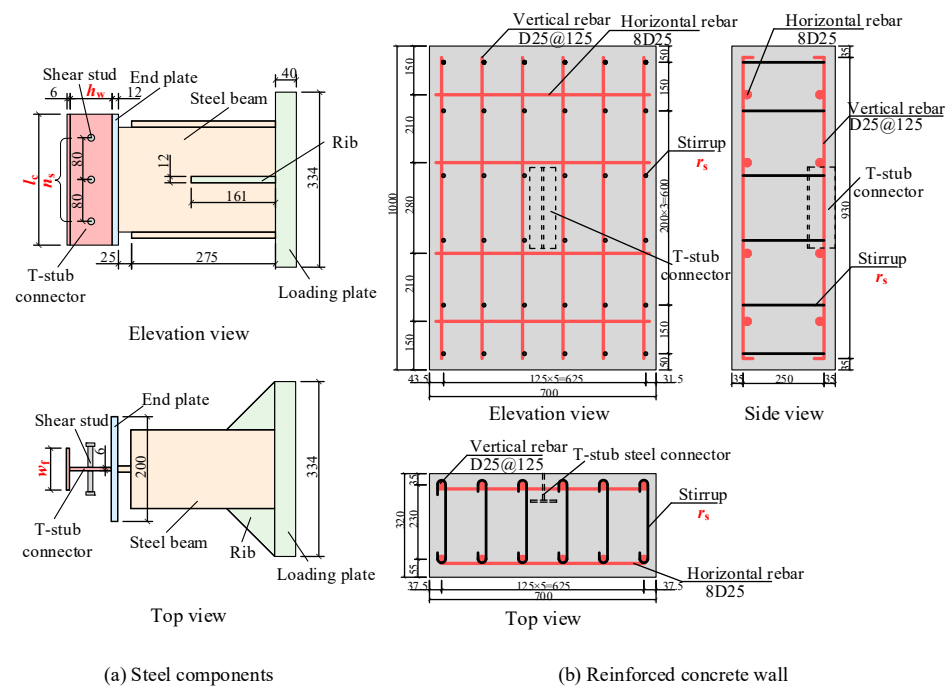
(a) Steel components   (b) Reinforced concrete wall

Figure 3. Geometric information of SBCW joints (unit: mm).

Table 1. The investigated parameters of the tested SBCW joint specimens [17].

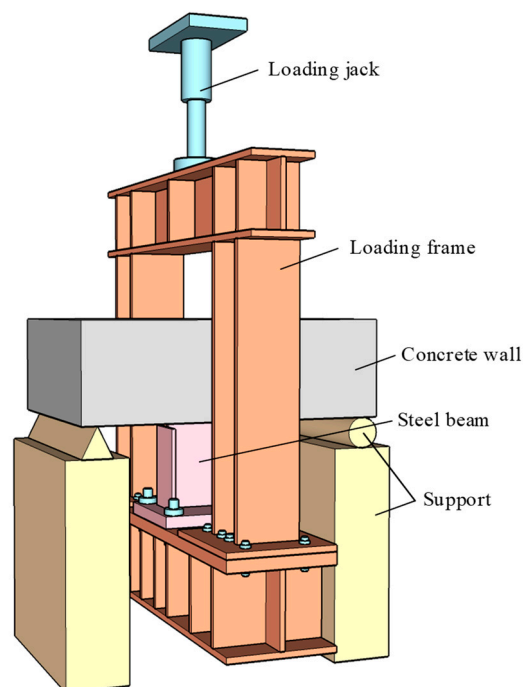| Specimen No.	l_c (mm)	w_f (mm)	h_w (mm)	n_s	r_s (%)
BWPJ-1	250	80	80	0	0.6
BWPJ-2	250	80	80	0	0.9
BWPJ-3	250	80	80	2	0.6
BWPJ-4	250	80	80	6	0.6
BWPJ-5	250	80	250	0	0.6
BWPJ-6	250	80	250	6	0.6

Figure 4. Test setup [17].

The numerical models of the steel components, concrete wall and reinforcements in SBCW joints are shown in Figure 5. Shell element 75, which is a four-node, thick-shell element with global displacements and rotations as degrees of freedom, was adopted for the steel plates of the steel beam, end plate and T-stub connector, as shown in Figure 5a. Considering that the loading plate is 40 mm thick and no local buckling occurred at the loading point, solid element 7, an isoparametric and arbitrary eight-node hexahedral element, was used for the loading plate. Since the concrete wall was in a three-dimensional complex stress state, solid element 7 was also utilised for the concrete. A 6 mm-thick gap was left in the concrete wall at the location of the web and flange of the T-stub connector, as marked in Figure 5b. Truss element 9, a simple two-node linear straight truss with three translational degrees of freedom, was used for the reinforcements including horizontal rebars, vertical rebars and stirrups, as shown in Figure 5c. Rectangular and cubic mesh types were used for the shell and solid elements, respectively, in order to achieve satisfactory computational convergence.
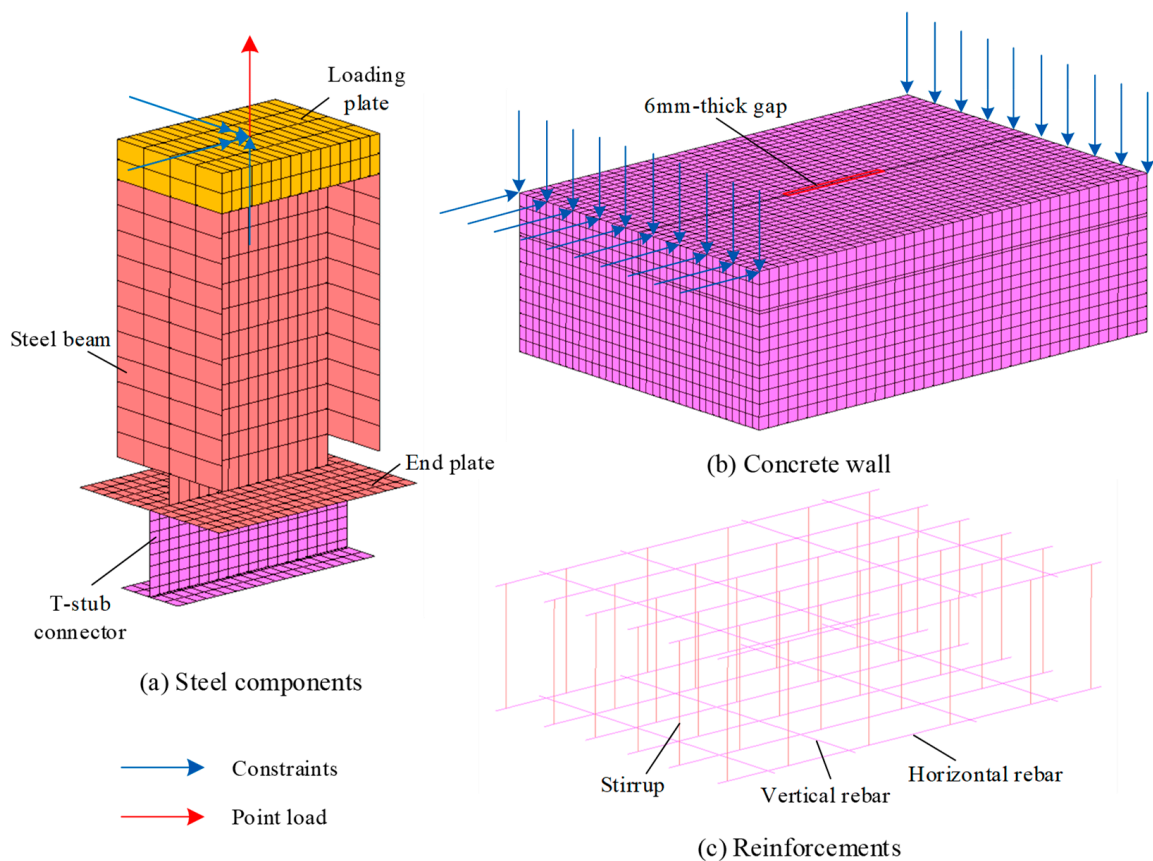

Figure 5. Numerical model of SBCW joints.

The mesh size was determined based on an analysis of mesh sensitivity [21,22]. Figure 6a shows the load-displacement curves of the numerical model of specimen BWPJ-1 with different mesh sizes. The comparison indicates that when the mesh size decreases to 20 mm, the effect of the mesh size can be ignored. Therefore, the mesh size of the main components including the T-stub connector, end plate, concrete wall and reinforcements, which have been shown to contribute to the pulling resistant capacity of the joints [17], was set as 20 mm. Figure 6b compares the curves of the models with different mesh sizes of the steel beam and loading plate, which suffered little damage during the tests. It can be seen that the mesh size of the steel beam and loading plate had little influence on the simulation results. Therefore, the mesh size of 40 mm was selected for the steel beam and loading plate for higher computational efficiency. Then, the number of elements could

be determined based on the mesh size. The number of shell elements was about 760 for specimens BWPJ-1~BWPJ-4 and 1020 for specimens BWPJ-5 and BWPJ-6. The approximate number of truss elements was 1700 for specimen BWPJ-2 and 1100 for the others. Since the geometric sizes of the concrete wall and loading plate remained unchanged in all cases, the number of solid elements was about 21,000 for all the specimens.
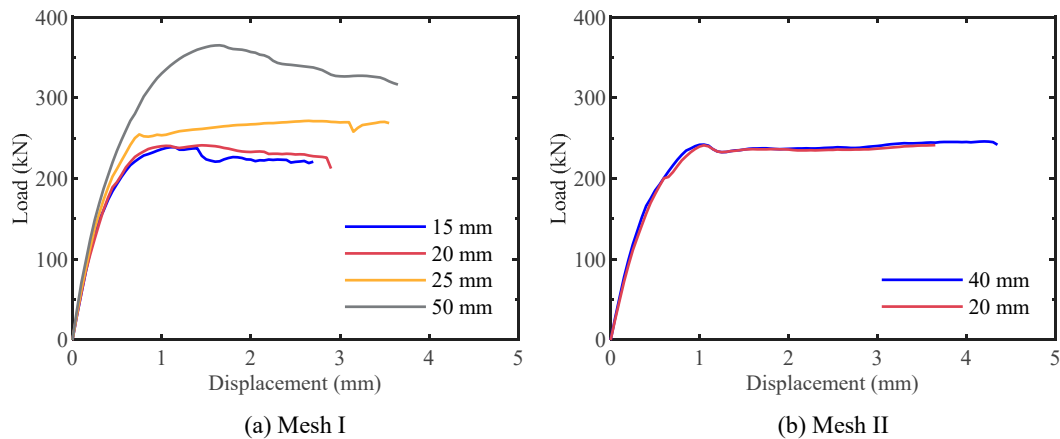

(a) Mesh I   (b) Mesh II

Figure 6. Mesh sensitivity analysis.

The boundary conditions of the finite element model are shown in Figure 5b: the out-of-plane displacement was restrained at the two ends of the concrete wall and the horizontal displacement was restrained at one end of the concrete wall to achieve similar boundary conditions to those in the experiments. Moreover, a slowly and uniformly increasing displacement load was applied to the central node of the loading plate in the pull-out direction, with the displacements in the other five directions all restrained, as illustrated in Figure 5a.

3.2. Material Properties

The material property tests [17] indicate that there was no obvious hardening effect after the yield stage in the steel and reinforcement materials. Therefore, a perfectly elastic-plastic constitutive model with the von Mises yielding surface was selected for the steel. The yield strength f_y of steel plates with different thicknesses and reinforcements with different diameters has been given in [17]. The elasticity modulus of steel and reinforcement materials was taken as 2.06×10^5 MPa and the Poisson's ratio is 0.3.

The uniaxial compressive stress-strain curve for concrete proposed by Hognestad et al. [23], as shown in Figure 7a, was adopted with the following two-stage expressions:

$$\sigma = \begin{cases} \sigma_0 \left[2\left(\frac{\varepsilon}{\varepsilon_0}\right) - \left(\frac{\varepsilon}{\varepsilon_0}\right)^2 \right], (0 < \varepsilon < \varepsilon_0) \\ \sigma_0 \left(1 - \eta_d \frac{\varepsilon - \varepsilon_0}{\varepsilon_{cu} - \varepsilon_0} \right), (\varepsilon_0 < \varepsilon < \varepsilon_u) \end{cases} \tag{1}$$

where σ and ε denote the stress and strain of concrete, respectively; σ_0 and ε_0 are the corresponding stress and strain values of concrete at the peak point of the curve, and σ_0 is equal to the cylinder compressive strength of concrete f_c' and $\varepsilon_0 = 2\sigma_0/E_c$ where E_c is the modulus of elasticity of concrete; ε_u is the ultimate strain of concrete taken as the recommended value of 0.0038, and η_d is the strength reduction factor, which was suggested to be 0.15 [23]. In order to consider the compressive failure of concrete, the crushing strain in the *Damage Effect* module of MSC.MARC [24] was set to the strain value when the stress decreases to $0.1 f_c'$. The cylinder compressive strength was calculated from the cubic compressive strength f_{cu} as follows:

$$f_c' = 0.8 f_{cu}. \tag{2}$$

The average cubic compressive strength of concrete for the six specimens has been given in [17]. As per CEB-FIP Model Code [25], the modulus of elasticity of concrete E_c can be determined based on the following equation:

$$E_c = \alpha_E E_{c0} \left(\frac{f_c'}{10} \right)^{1/3} \tag{3}$$

where $E_{c0} = 21.5 \times 10^3$ MPa and $\alpha_E = 1.0$ for quartzite aggregates used in the test specimens. The Poisson's ratio of concrete is 0.2. The von Mises yield criterion and isotropic hardening rule in the *Plasticity Property* module of MSC.MARC [24] were implemented for concrete.
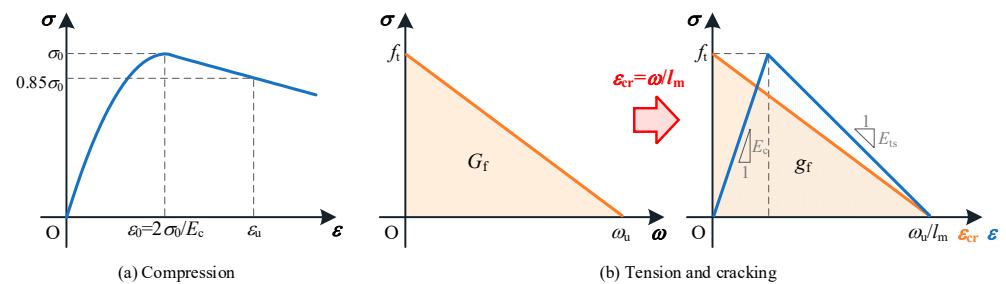

Figure 7. Uniaxial constitutive law for concrete.

The smeared crack model with fixed angle crack assumption [26] was utilised to model the tensile behaviour of concrete. The crack bond theory proposed by Bažant and Oh [27] was adopted to reduce the size effect on the simulation results. The tensile softening behaviour can be described using the uniaxial stress σ-crack width ω curve as illustrated in Figure 7b. The fracture energy G_f equals to the area enclosed by the σ-ω curve and the coordinate axes, which represents the energy dissipated per unit cross-sectional area during the propagation process of a concrete crack. The fracture energy of concrete is affected by many factors, including the water/cement ratio, the maximum aggregate size, the age of concrete, curing conditions, the size of a structural member and, in particular, the depth of the ligament above a crack or notch [25]. Previous studies [25,27–31] proposed different formulas for the fracture energy considering one or several of the factors mentioned above. When there is no experimental data specifically for concrete tensile behaviour, the values of fracture energy are generally determined [32–34] according to CEB-FIP Model Code [25,31]. The 2010 version of CEB-FIP Model Code [25] recommends that the fracture energy can be calculated as follows:

$$G_f = 0.073 \left(f_c' \right)^{0.18}. \tag{4}$$

The concrete tensile strength f_t, the stress corresponding to the initial cracking point, can be obtained by the following equation [25]:

$$f_t = \begin{cases} 0.3(f_c' - 8)^{2/3}, f_c' \leq 58 \text{ MPa} \\ 2.12 \ln(1 + 0.1 f_c'), f_c' > 58 \text{ MPa} \end{cases}. \tag{5}$$

Based on the conversion from the σ-ω curve to the σ-ε_{cr} (ε_{cr} denotes the cracking strain of concrete) curve shown in Figure 7b, the tensile softening modulus E_{ts} and the ultimate tensile strain ε_{tu} of concrete can be derived as follows:

$$E_{ts} = \frac{1}{\frac{2G_f}{f_t^2 l_m} - \frac{1}{E_c}} \tag{6}$$

$$\varepsilon_{tu} = \frac{2G_f}{f_t l_m} \tag{7}$$

where l_m is the width of the smeared crack bond and also the mean crack spacing. For reinforced concrete members, the mean crack spacing can be determined by the following equation [35]:

$$l_m = \beta(1.9c + 0.08\frac{d_{eq}}{\rho_{te}}) \tag{8}$$

where the coefficient β is set as 1.0 for concrete walls; c is the concrete cover depth, set as an average value of 47.5 mm in this case; and d_{eq} and ρ_{eq} are the equivalent diameter and the reinforcement ratio of effective rebars in tension, respectively.

The shear retention factor η is the ratio of the shear modulus of cracked concrete to the elastic shear modulus of intact concrete. In order to avoid the shear locking effect in the fixed angle crack model, a changing shear retention factor [36,37] was implemented for the shear behaviour analysis of concrete, which is expressed as:

$$\eta = \eta_0 \cdot \exp(-m \cdot \varepsilon_{cr}) \tag{9}$$

where η_0 is the initial shear retention factor; and m is a parameter controlling the decreasing rate of the shear retention factor with the increase in cracking strain. In the numerical model, η_0 was set as 0.25 and m was set as 800, which are suggested by Tao and Nie [38] based on an analysis of a large number of experimental and numerical results.

3.3. Interface

Since the T-stub connector is embedded in the concrete wall to transfer the pull-out force from the steel beam, the modelling techniques of interfaces between the steel plates of the T-stub connector and the concrete should be carefully considered to accurately simulate the mechanical performance of the joints. Considering that there is mainly compression between the flange plate of the T-stub connector and the upper concrete, and no obvious slide or separation occurred during the loading process, the common node strategy was adopted, as shown in Figure 8a, to ensure all of the freedoms of the nodes were tied together, which is a reasonable and allowable simplified modelling approach [34]. For specimens BWPJ-3, BWPJ-4 and BWPJ-6 in which the shear studs are arranged on the web plate of the T-stub connector, the spring link was set in the tangential direction between the web plate and the concrete on both sides, as shown in Figure 8b. A nonlinear model proposed by Ollgaard et al. [39] was implemented to simulate the shear behaviour of shear studs, which is expressed as follows:

$$V = V_u(1 - e^{-ns})^m \tag{10}$$

where V is the shear force of studs; s is the slide displacement; m and n are set as the common values 0.558 and 1 mm^{-1}, respectively; and V_u is the ultimate shear capacity of studs, which can be calculated as [40]:

$$V_u = 0.43A_s\sqrt{E_cf_c} \le 0.7A_sf_u \tag{11}$$

where A_s is the cross-sectional area of the stud rod; f_c is the prism compressive strength of concrete determined by $f_c = 0.76f_{cu}$, and f_u is the ultimate tensile strength of studs, taken as 420 MPa in this case based on the code *Cheese Head Studs for Arc Stud Welding* [41]. In addition, since the shear studs have good pulling resistant capacity, the nodes of the web plate of the T-stub connector and concrete at the location of shear studs were tied together in the normal direction. Considering that the friction between steel and concrete is so minimal that it has little contribution to the pulling resistant capacity of joints, no links or ties were set between the web plate and concrete where there were no shear studs arranged.
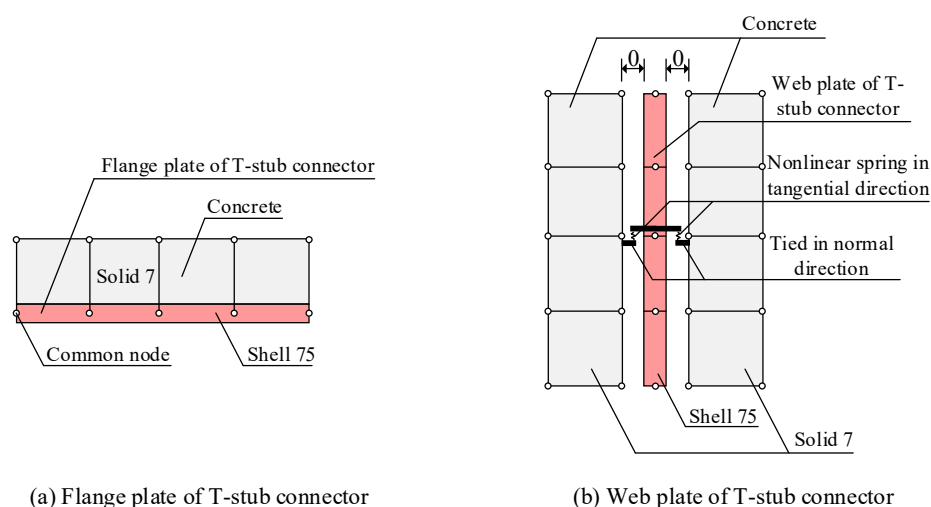
(a) Flange plate of T-stub connector   (b) Web plate of T-stub connector

Figure 8. Modelling of interfaces between steel plates and concrete.

Moreover, the common node strategy was also adopted for the interface between the reinforcements and concrete, which has been found to have similar simulation results to the 'insert' model in MSC.MARC [24], but can achieve better convergence through trials. The tests continued until obvious deformation and severe damage of the specimens were observed, in which situation the nonlinearity was significant. Therefore, the 'large strain', which activates a formulation suitable for large strains, large displacements and large rotations using the updated Lagrange framework for elements and materials by default [24], was selected in the *Structural Analysis Options* module to consider the geometric and material nonlinearity [34].

4. Numerical Modelling Results

4.1. Load-Displacement Curves

The load-displacement curves obtained from the numerical models for the six specimens are compared with the test results in Figure 9. The initial stiffness of numerical results is a little larger than that of test results for specimens BWPJ-1~BWPJ-4, which demonstrated the concrete breakout failure mode. This is probably because the finite element model overestimates the shear modulus of concrete despite a modified shear retention factor having been implemented. The differences between the numerical and test curves of specimen BWPJ-2 are more pronounced than those of the other three specimens, because the measured pull-out displacements of specimen BWPJ-2 are larger at the same load level. The differences are probably caused by errors in the displacement meter or the initial gap between the specimen and the supports. Although the experimental displacement of specimens BWPJ-5 and BWPJ-6 is smaller than that of the other specimens due to early termination of loading, the former part of the numerical curves fits well with the test curves for the two specimens with the steel web yield failure mode. The pulling resistant capacities of all specimens obtained from the test results and numerical results are listed in Table 2. The numerical capacity of specimen BWPJ-4 is lower than the test value, which is possibly caused by underestimation of the shear capacity of studs, considering that there is no actual test data about the strength of studs. Additionally, since the load capacity of specimen BWPJ-5 may not reach the peak point because of early termination, the predicted capacity by the finite element model of specimen BWPJ-5 is a little higher than the test result. The overall comparison between the numerical and test results indicates that the numerical models can predict the load-deformation process, especially the pulling resistant capacity, with good accuracy. Therefore, the modelling approach of SBCW joints proposed in this study is reliable and reasonable.
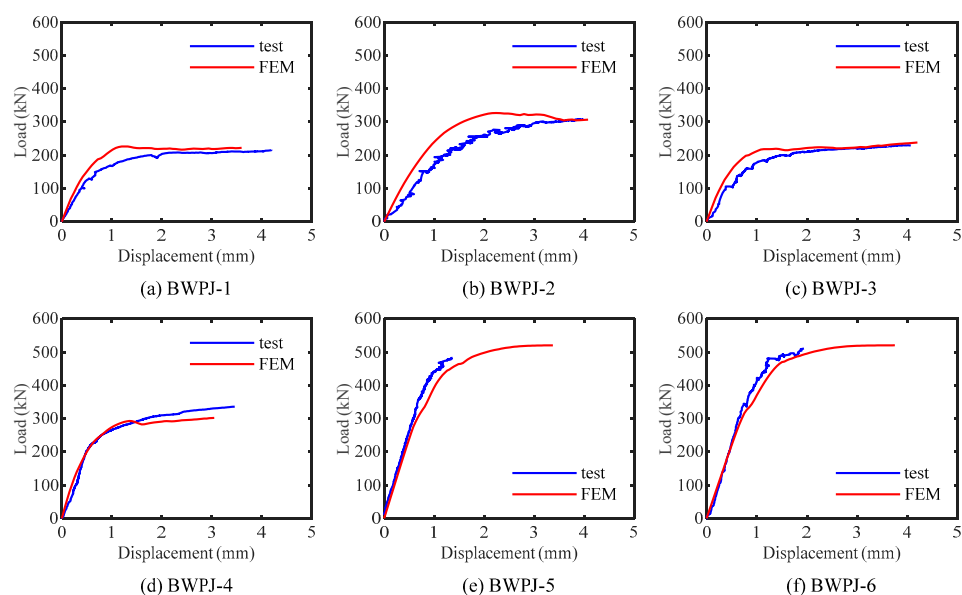
Figure 9. Load-displacement curves.

Table 2. Comparison of pulling resistant capacity of test specimens.

Specimen No.	Failure Mode	P_T (kN) [1]	P_{FEM} (kN) [2]	err_{FEM} [3]
BWPJ-1	Concrete breakout	216.7	226.2	4.4%
BWPJ-2	Concrete breakout	311.5	326.6	4.8%
BWPJ-3	Concrete breakout	230.3	238.0	3.3%
BWPJ-4	Concrete breakout	343.3	302.2	−12.0%
BWPJ-5	Steel web yield	482.4	520.2	7.8%
BWPJ-6	Steel web yield	510.5	520.3	1.9%
AVE [4]		-	-	1.7%
STD [5]		-	-	6.4%

[1] P_T is the pulling resistant capacity obtained from the tests. [2] P_{FEM} is the pulling resistant capacity predicted by the finite element model. [3] err_{FEM} is the error of numerical results relative to the test results. [4] AVE is the average value. [5] STD is the standard deviation.

4.2. Strain and Stress Development of the T-stub Connector

During the loading process, the web plate of the T-stub connector was in a nearly pure tension state, and the tensile strain in the outer and central zones was measured by strain gauges. The tensile strain at the same location of the web plate is extracted from the analysis results of the finite element models and compared with the test data in Figure 10. For all specimens, the tensile strain in the outer zone is larger than that in the central zone, which can be well predicted by the numerical models. The numerical strain of specimens BWPJ-1~BWPJ-4 is larger than the test value at the same load level, but the deviation can be tolerated considering the inaccuracy of strain measurement. The tensile strain of specimens BWPJ-5 and BWPJ-6 exceeded the yield strain, indicating that the web plates of the two specimens yielded. The numerical models can predict the yielding of web plates and the yield point more obviously than the test curves because the perfectly elastic-plastic constitutive model is used for steel materials. In general, finite element models can capture the main characteristics of the strain development of the web plates. Strain analysis shows that the web plates of specimens BWPJ-1~BWPJ-4 remained elastic while those of specimens BWPJ-5 and BWPJ-6 yielded under pull-out loads.
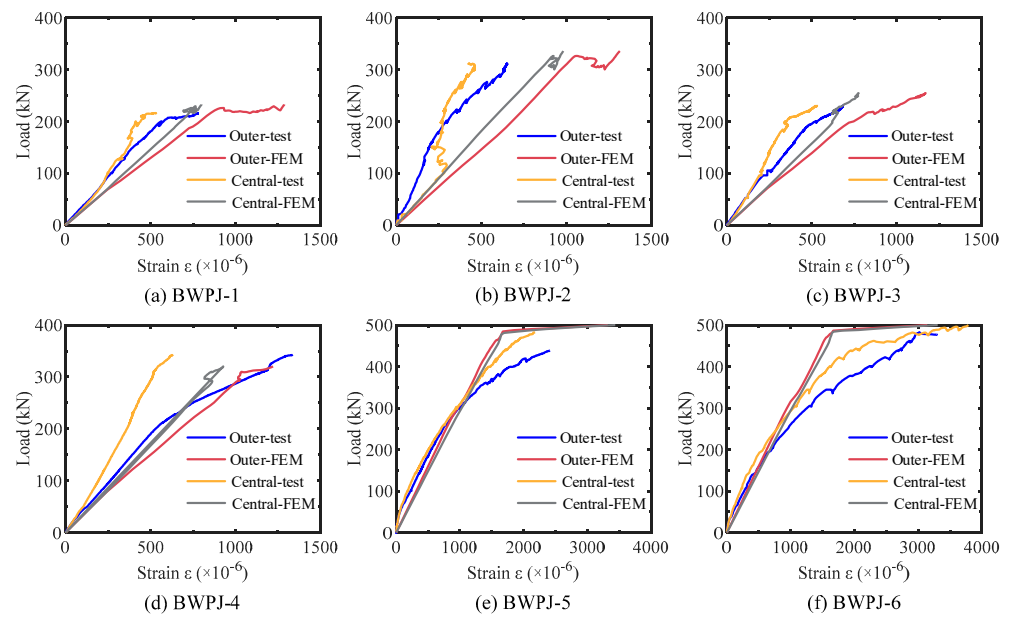
Figure 10. Strain development curves of the web plate of the T-stub connector.

The equivalent von Mises stress curves of the flange plate of the T-stub connector in the outer and central zones obtained from the numerical results and test results are illustrated in Figure 11. Similar to the web plates of the T-stub connector, the stress in the outer zone develops faster than in the central zone due to different constraint conditions. In addition, the stress of specimens BWPJ-5 and BWPJ-6, which are subjected to larger pull-out action, is larger than that of specimens BWPJ-1~BWPJ-4. The numerical stress is smaller than the test stress for specimens BWPJ-1~BWPJ-4, which is probably caused by the common node modelling strategy leading to a slight underestimation of the deformation of flange plates. Nevertheless, the strain and stress development of the T-stub connector obtained from the numerical models fit the experimental results reasonably well, which provides a good basis for further analysis of the pull-out behaviour of the SBCW joint.
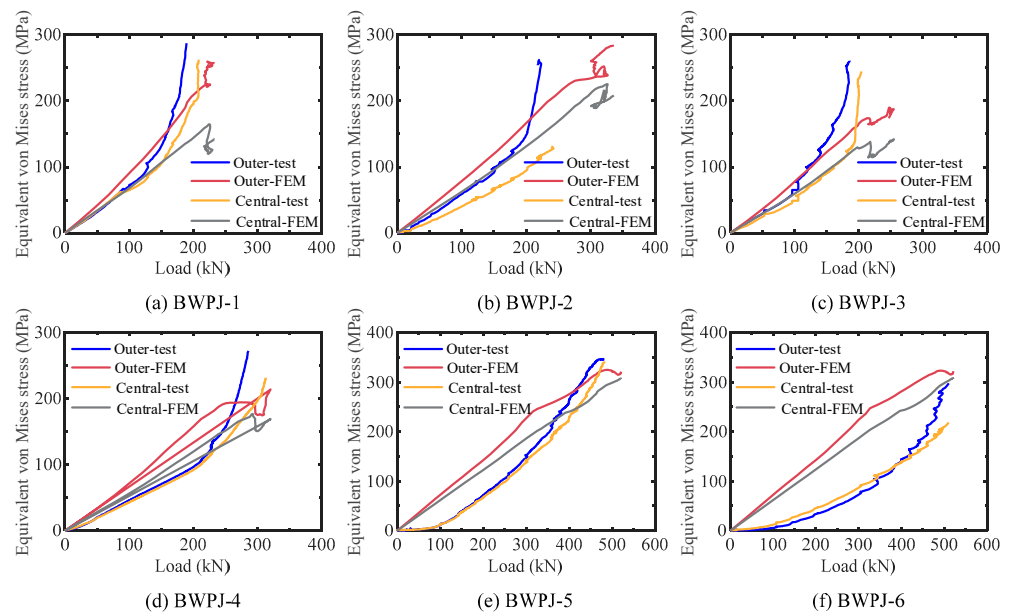
Figure 11. Stress development curves of the flange plate of the T-stub connector.

4.3. Stress Development of the Stirrups

Figure 12 shows the tensile stress development of the stirrups in the joint core area. For both test results and numerical results, the stress of the stirrups first increases rapidly and then slowly with the increasement of the pull-out displacement of the joint. The inflection point of the stirrup stress development curves coincides with the yield point of the specimens. The stirrup stress of specimens BWPJ-5 and BWPJ-6 is much smaller than that of the other four specimens, indicating that the stirrups make little contribution to the pulling resistant capacity of the SBCW joints with the steel web yield failure mode. For specimens BWPJ-1~BWPJ-4, since the concrete in the joint core area experiences large deformation and damage, the stirrups participate in the pulling resistant mechanism, presenting higher stress level.

(a) BWPJ-1

(b) BWPJ-2

(c) BWPJ-3

(d) BWPJ-4

(e) BWPJ-5

(f) BWPJ-6
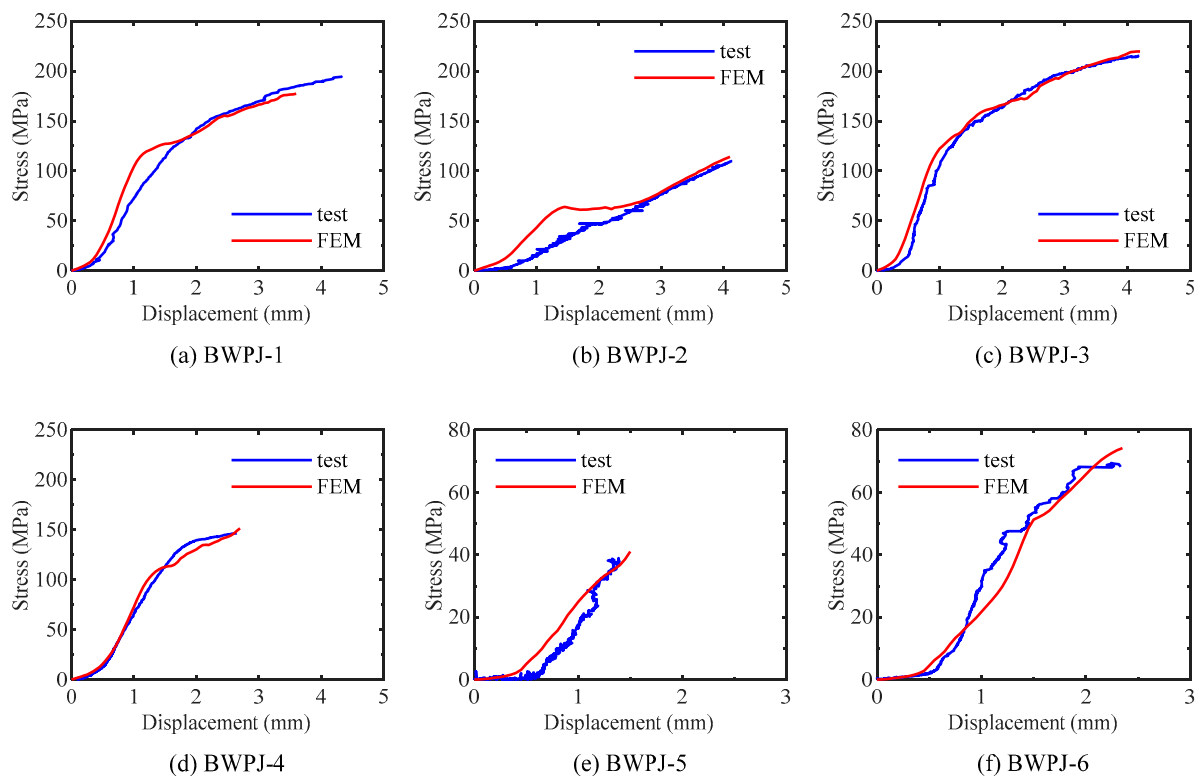
Figure 12. Stress development curves of the stirrups.

4.4. Pull-Out Deformation

The difference between the displacements at the center of the end plate and the concrete wall surface obtained from the numerical models for all the specimens is illustrated in Figure 13. Since the end plate is welded to the web plate of the connector, the displacement difference can represent the relative locations of the T-stub connector and the concrete wall. For specimens BWPJ-1~BWPJ-4, the displacement difference changes little during the loading process. However, the displacement difference of specimens BWPJ-5 and BWPJ-6 exhibits a significant rise with the increasement of the pull-out displacement of the joint. The characteristic deformation patterns of the two groups of specimens at the failure point are shown in Figure 14. It is indicated that the pull-out deformation is concentrated in the concrete wall for the first four specimens while in the T-stub connector, especially the web plate, for the last two specimens, which is consistent with the corresponding failure modes of these specimens.
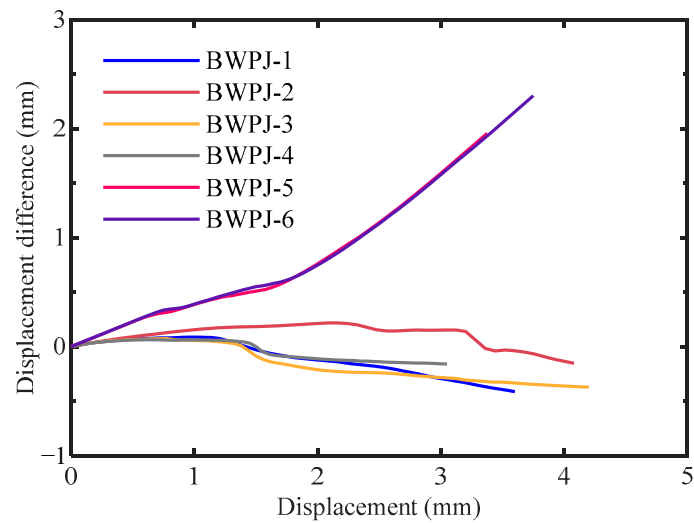
Figure 13. Displacement difference between the center of the end plate and the concrete wall surface.

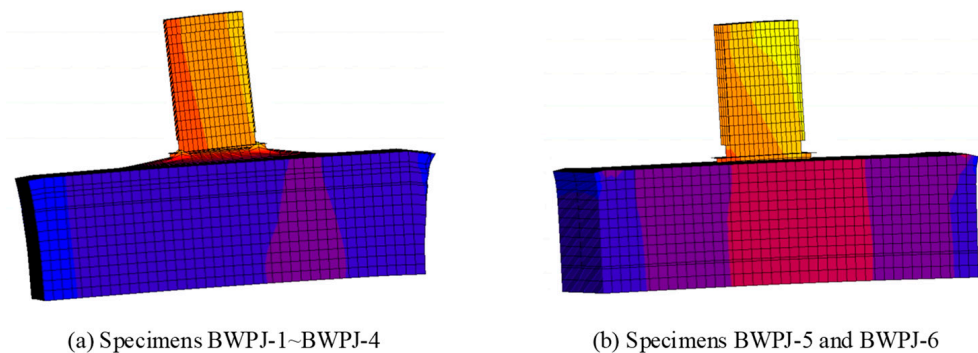(a) Specimens BWPJ-1~BWPJ-4   (b) Specimens BWPJ-5 and BWPJ-6

Figure 14. Two characteristic deformation patterns (Deformation scaling factor = 15).

4.5. Failure Mode

The stress states of the steel components and crack patterns of the concrete wall of each specimen were analysed in order to investigate the failure modes of SBCW joints. Figure 15 shows the equivalent von Mises stress distribution of the steel components at the failure point with the largest stress value marked at the corresponding location. It can be seen that the stress in the web plate of the T-stub connector is the highest among the steel components, indicating that the web plate of the connector is the weakest part when the joint is under tension. The maximum stress of specimens BWPJ-5 and BWPJ-6 is higher than that of specimens BWPJ-1~BWPJ-4, and the web plates of specimens BWPJ-5 and BWPJ-6 are at a high stress level. It is demonstrated that the web plates of the connector in the last two specimens suffered more serious damage than those in the other four specimens.

The equivalent cracking strain of the concrete wall marked with the largest strain value at the failure point is presented in Figure 16. In order to observe the internal concrete cracking more clearly, the concrete wall was dissected at one end of the T-stub connector to show the strain distribution. It can be seen that the cracking strain of specimens BWPJ-1~BWPJ-4 is significantly larger than that of specimens BWPJ-5 and BWPJ-6, indicating that the concrete in the first four specimens suffered serious damage under pull-out load. What's more, the concrete cracking strain in specimens BWPJ-1~BWPJ-4 concentrates in the strips extending from the flange of the T-stub connector to the surface of the concrete wall, revealing the breakout failure zone of the concrete.
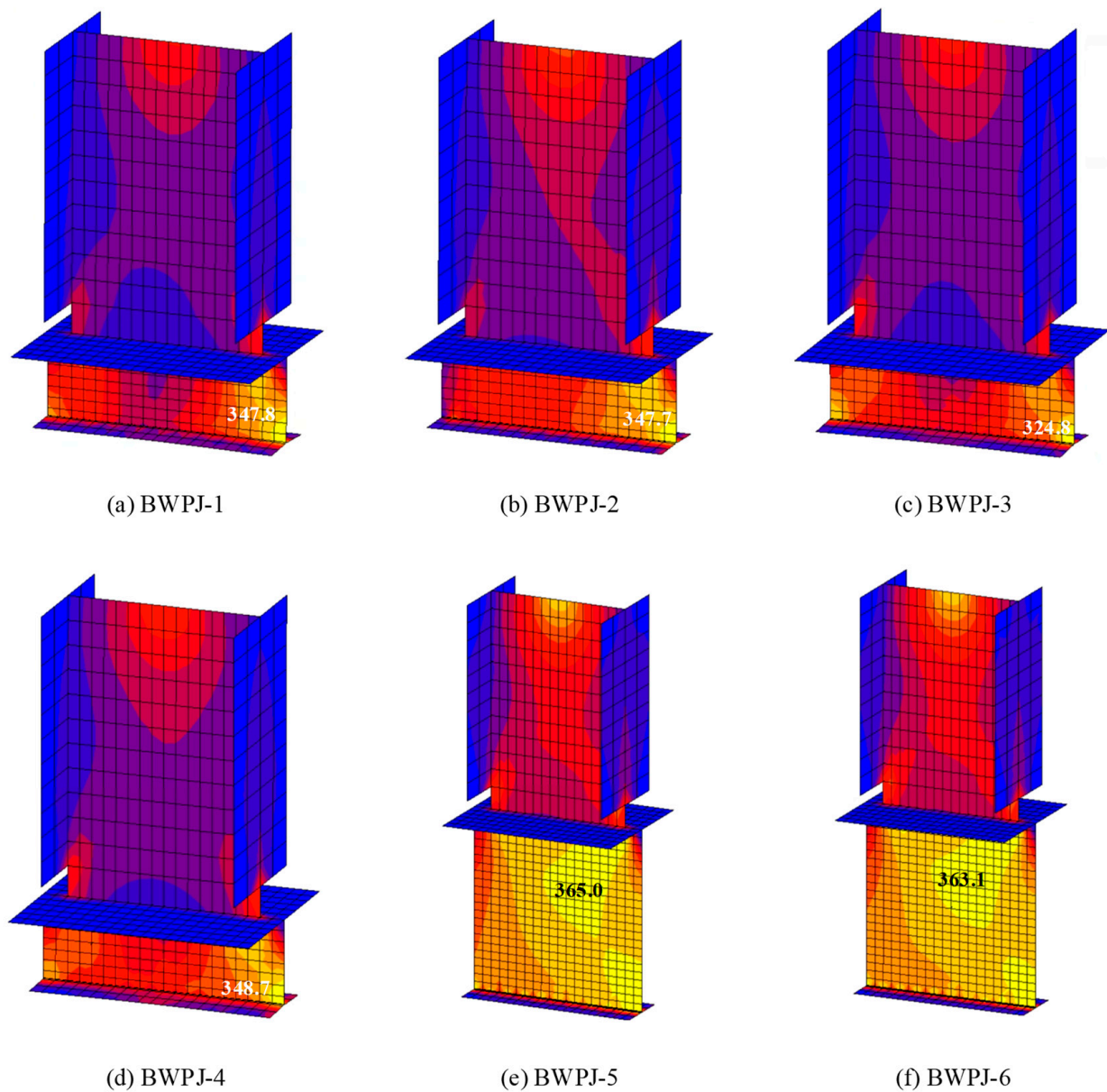
(a) BWPJ-1   (b) BWPJ-2   (c) BWPJ-3

(d) BWPJ-4   (e) BWPJ-5   (f) BWPJ-6

Figure 15. Equivalent von Mises stress (MPa) of the steel components at the failure point.

In conclusion, the stress and strain distribution of the steel components and concrete wall demonstrates that the two failure modes of the SBCW joints have totally different characteristics: For the concrete breakout failure mode of specimens BWPJ-1~BWPJ-4, the stress of the concrete in the joint core area is high, and a pyramid is formed and pulled out resulting in a brittle failure of the joint; for the steel web yield failure mode of specimens BWPJ-5 and BWPJ-6, the concrete remains intact with very low cracking strain, while the web plate of the T-stub connector yields under tension leading to a ductile failure of the joint.

(a) BWPJ-1   (b) BWPJ-2   (c) BWPJ-3

(d) BWPJ-4   (e) BWPJ-5   (f) BWPJ-6
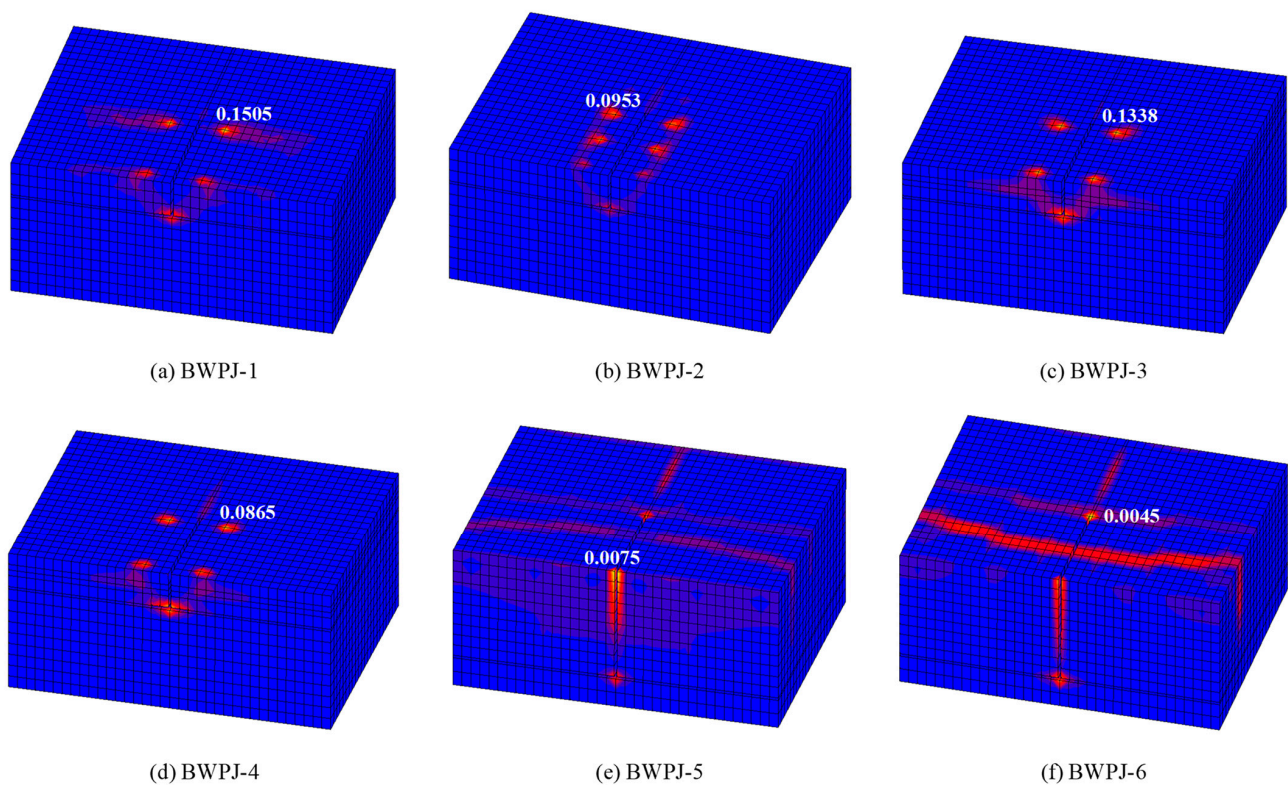
Figure 16. Equivalent cracking strain of the concrete wall at the failure point.

5. Parametric Analyses

In this section, simulations of cases with various parameters based on the numerical model are conducted to investigate the influences of different parameters on the pulling resistant capacity and propose suggestions for the design of SBCW joints. Specimen BWPJ-1 is chosen as the basic model for the parametric analyses.

5.1. Length of the T-stub Connector l_c

The load-displacement curves of the joints with different lengths of the T-stub connectors are illustrated in Figure 17. It can be clearly seen that the connector length has a large effect on the pull-out behaviour of the joint. When the length of the T-stub connector l_c is small, the joint exhibits smaller stiffness and lower capacity. The strength and stiffness of the joint increase uniformly with the rise in the connector length. Moreover, the concrete breakout failure mode is observed for all four models with l_c in the range of 100 mm to 250 mm. Therefore, the SBCW joint with a longer T-stub connector can meet the demand for higher design capacity if the concrete breakout failure is allowed. However, the length of the T-stub connector should be smaller than the space between the horizontal rebars to avoid conflict between the connector and the reinforcements in the design of the joint.
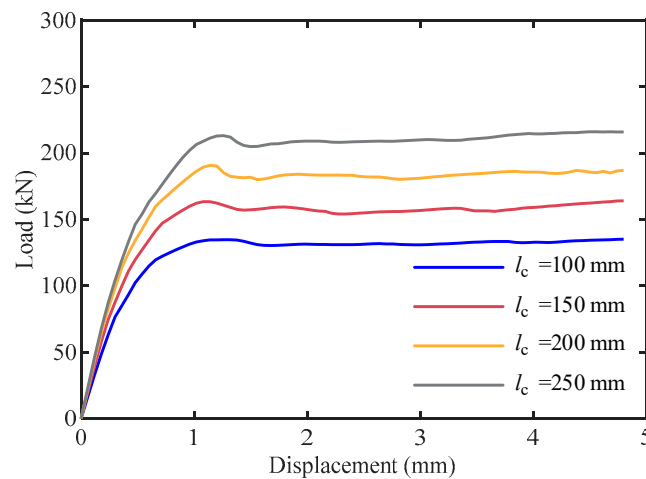
Figure 17. Influence of the length of the T-stub connector.

5.2. Flange width of the T-stub Connector w_f

The influence of the flange width of the T-stub connector w_f is shown in Figure 18. There are few differences among the load-displacement curves of the joints with w_f in the range of 40 mm to 120 mm, and the concrete breakout failure occurs in all models. The initial stiffness is nearly the same. Despite a few changes observed in the ultimate capacity, no clear conclusions can be drawn on the relationship between the flange width of the T-stub connector and the loading capacity of the joint. Considering that the maximum relative difference among the capacity of these cases is only 7.7%, the influences of the flange width of the T-stub connector on the pull-out behaviour of SBCW joints can be ignored.
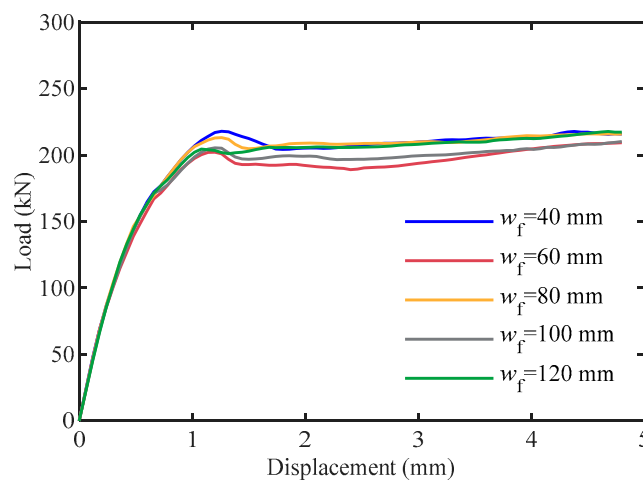
Figure 18. Influence of the flange width of the T-stub connector.

5.3. Number of Shear Studs n_s

The influence of the number of shear studs on the web plate of the T-stub connector n_s is shown in Figure 19. The shear studs are arranged symmetrically on both sides of the web plate, and four cases with the total numbers of shear studs as 0, 2, 4 and 6 are analysed considering the size of the web plate. The concrete breakout failure is observed in all four models. The comparison of the load-displacement curves indicates that the arrangement of shear studs can effectively increase the stiffness and pulling resistant capacity of the joint. The contribution of shear studs can be explained by the theoretical model proposed by Zhao et al. [17] wherein the shear studs go through the punching failure surface of the concrete in the joint core area.
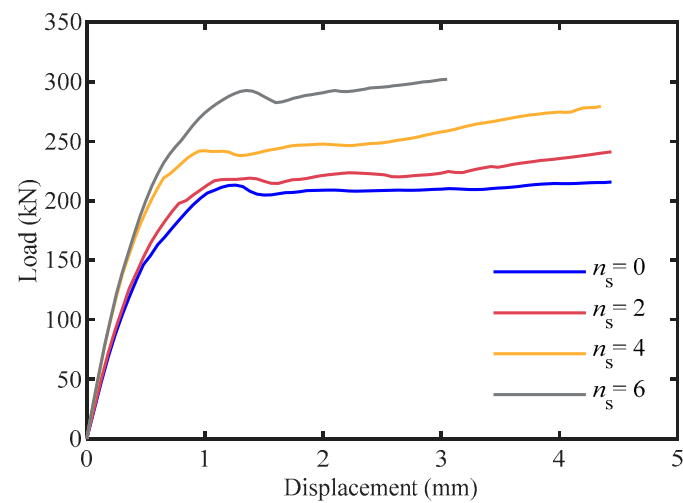
Figure 19. Influence of the number of shear studs.

5.4. Reinforcement Ratio of Stirrups r_s

The influence of the reinforcement ratio of stirrups r_s is shown in Figure 20. Four cases with r_s ranging from 0.39% to 0.97% are simulated and all models demonstrate the concrete breakout failure mode. When the reinforcement ratio of stirrups is relatively small, the encryption of stirrups has a significant influence on the loading capacity of SBCW joints. However, the enhancement effect is not obvious when r_s is larger, indicating that there is an optimal reinforcement ratio of stirrups for the concrete breakout failure mode, which is approximately 0.7~0.8% in this case. In addition, the reinforcement ratio of stirrups has little effect on the initial stiffness of the joint.
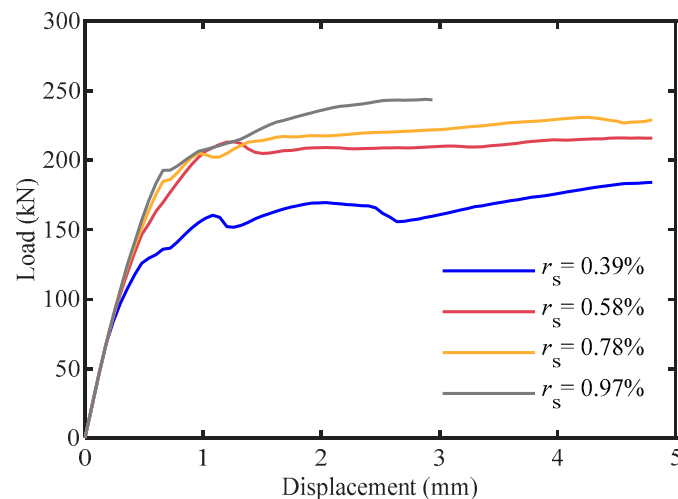
Figure 20. Influence of the reinforcement ratio of stirrups.

5.5. Web Height of the T-stub Connector h_w

The load-displacement curves of the SBCW joints with different web heights of the T-stub connectors are plotted in Figure 21. It can be observed that the pulling resistant capacity increased significantly with the increasement of the web height of the connector h_w, and concrete breakout failure occurs when h_w is relatively small. Nevertheless, when h_w increases to a certain level, the load-displacement curve no longer rises, and steel web yield failure is observed at the ultimate point of the joint. The changes of the characteristics of the load-displacement curves and the failure mode indicate that the web height of the connector is a critical parameter for the pulling-resistant behaviour of SBCW joints. An explanation for this phenomenon is that the pyramid of the concrete breakout failure mode

is difficult to form when the embedded depth of the connector, which equals h_w, is large enough, so that the failure of the SBCW joint is dominated by the steel web failure mode.
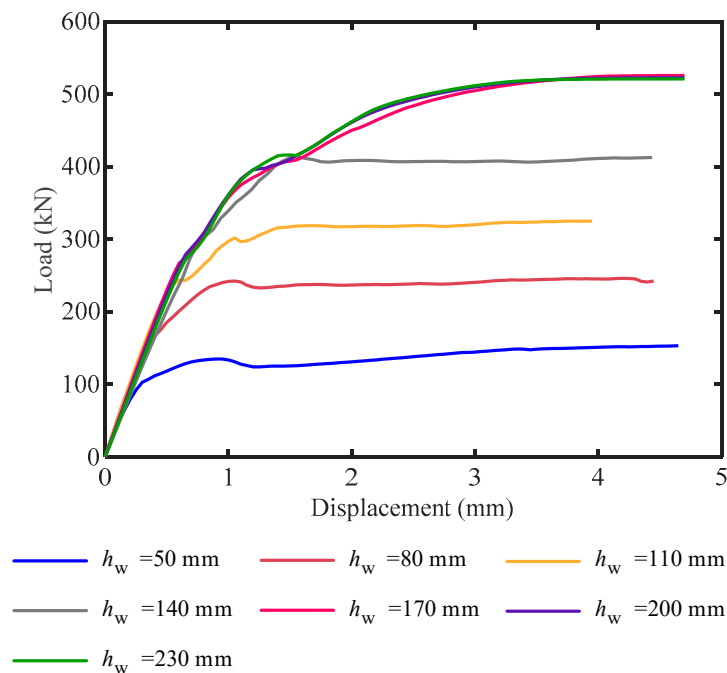

Figure 21. Influence of the web height of the T-stub connector.

6. Discussion on the Critical Embedded Depth of the T-stub Connector

The parametric analyses indicate that the failure mode of SBCW joints is mainly determined by the embedded depth of the T-stub connector. The steel web yield failure, which demonstrates higher capacity and better ductility, is the more favourable failure mode in the design of SBCW joints. The analysis results in Section 4.5 show that with the increase in the embedded depth, the failure mode changes from the concrete breakout failure to the steel web yield failure. Therefore, there exists a critical embedded depth of the T-stub connector, denoted by d_c. When the embedded depth of the T-stub connector d is smaller than d_c, the pulling resistant capacity corresponding to the concrete breakout failure is lower than that of the steel web yield failure, so that concrete breakout failure occurs. When d is larger than d_c, the capacity of the steel web yield failure is lower, and this failure becomes the actual failure mode.

In order to determine the critical embedded depth, the pulling resistant capacity of the SBCW joints with various embedded depths corresponding to the two failure modes are calculated using the theoretical model proposed in [17]. The capacity curves corresponding to the two failure modes are shown in Figure 22, and the numerical results of the seven models in Section 4.5 are also plotted to verify the theoretical results. It can be observed that there is an intersection point between the two capacity curves and the actual capacity curve consisting of the parts of the two curves located below plotted by solid lines. The horizontal coordinate corresponding to the intersection point is the critical embedded depth of the T-stub connector d_c, which is 166 mm in this case. If the design of the SBCW joints requires high capacity and good ductility, the embedded depth of the connector is recommended to be larger than d_c.
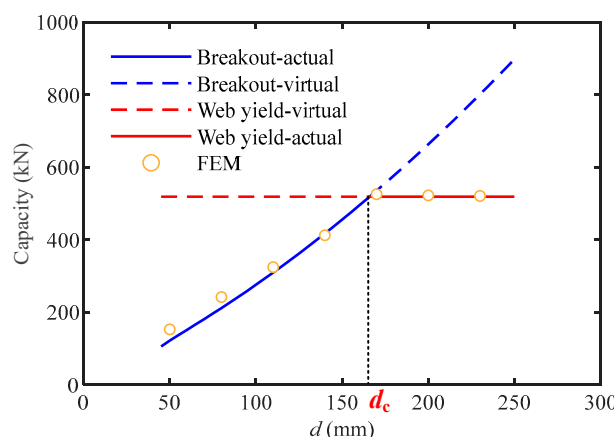
Figure 22. Pulling resistant capacity curves corresponding to the two failure modes.

7. Conclusions

The pulling resistant capacity of SBCW joints with T-stub connectors was investigated by numerical simulation. An elaborate 3D finite element model was established and validated using test results. Based on the numerical model, parametric analyses were carried out and the key design parameters of joints were determined. Finally, the critical embedded depth of the T-stub connector was determined to provide design references. The main conclusions of this study are drawn as follows:

(1) The load-displacement relationship, strain and stress development, deformation characteristics and failure modes of SBCW joints with T-stub connectors under pull-out load were studied in detail based on the finite element model. The pulling resistant capacity of joints with concrete breakout failure is obviously lower than with steel web yield failure. The numerical results indicate that the deformation and damage concentrate on the concrete and stirrups for concrete breakout failure, as well as on the web plate of the T-stub connector for steel web yield failure.

(2) The influences of main design parameters on the load-displacement curves of the joints were analysed. It is indicated that the length and the web height of the T-stub connector, the number of shear studs on the web plate of the connector and the reinforcement ratio of stirrups have obvious effects on the pulling resistant capacity of the joints with concrete breakout failure in a certain range. In addition, the web height of the connector, which is also the embedded depth, is the key parameter that determines the failure mode of the joint.

(3) The parametric analyses demonstrate that there exists a minimum embedded depth of the T-stub connector to achieve steel web yield failure. The critical value of the embedded depth for the basic joint is determined to be 166 mm using the theoretical model. In the design of SBCW joints, the embedded depth of the T-stub connector is suggested to be larger than the critical value to obtain higher pulling resistant capacity with a ductile failure mode. It should be noted that the critical value only applies to the joint with the dimensions in this study. The effects of a wider range of parameters on the critical embedded depth deserve further investigation.

References

1. Morino, S. Recent developments in hybrid structures in Japan—Research, design and construction. *Eng. Struct.* **1998**, *20*, 336–346. [CrossRef]
2. Shahrooz, B.M.; Gong, B.; Tunc, G.; Deason, J.T. An overview of reinforced concrete core wall-steel frame hybrid structures. *Prog. Struct. Eng. Mater.* **2001**, *3*, 149–158. [CrossRef]
3. Wang, D.S.; Zhou, J.L. Development and prospect of hybrid high-rise building structures in China. *J. Build. Struct.* **2010**, *31*, 62–70. (In Chinese)
4. Wallace, J.W.; Wada, A. Hybrid wall systems: US-Japan research. In Proceedings of the 12th WCEE Conference, Auckland, New Zeland, 30 January–4 February 2000.
5. Goel, S.C.; Tsai, K.C. Overview of International Cooperative Research on Seismic Performance of Composite and Hybrid Structures. In *Structures 2004: Building on the Past, Securing the Future*; ASCE: Reston, VA, USA, 2004; pp. 1–7.
6. Zhang, B.Q. Experimental research of the single plate framing connection between truss-steel beam and concrete wall. Master's Dissertation, Bejing University of Technology, Beijing, China, 2002. (In Chinese)
7. Liu, A.M.; Zhou, D.Y. Experimental study on seismic behavior of semi-rigid connection between steel beam and concrete wall. *Earthq. Eng. Eng. Vib.* **2005**, *4*, 129–137.
8. Hawkins, N.; Mitchell, D.; Roeder, C. Moment resisting connections for mixed construction. *Eng. J.* **1980**, *17*, 1–10.
9. Roeder, C.; Hawkins, N. Connections between steel frames and concrete walls. *Eng. J.* **1981**, *18*, 22–29.
10. Shahrooz, B.M.; Deason, J.T.; Tunc, G. Outrigger beam–wall connections. I: Component testing and development of design model. *J. Struct. Eng.* **2004**, *130*, 253–261. [CrossRef]
11. Shahrooz, B.M.; Tunc, G.; Deason, J.T. Outrigger beam–wall connections. II: Subassembly testing and further modeling enhancements. *J. Struct. Eng.* **2004**, *130*, 262–270. [CrossRef]
12. Li, G.Q.; Qu, B.; Sun, F.F.; He, W.M.; Guo, J.Y. Cyclic loading tests of steel beam to concrete wall joints in steel-concrete mixed structures. *J. Build. Struct.* **2003**, *24*, 1–7. (In Chinese)
13. Zhu, J. Study on behavior of connection between steel beam and concrete wall with embedded section steel. Ph.D. Dissertation, Wuhan University of Technology, Wuhan, China, 2006. (In Chinese)
14. Zhou, X.; Li, G. Shaking table model test of a steel-concrete composite high-rise building. *J. Earthq. Eng.* **2010**, *14*, 601–625. [CrossRef]
15. Zhao, H.; Tao, M.-X.; Ding, R. Experimental study on seismic behaviour of composite frames with wide floor slabs considering the effect of floor loads. *Eng. Struct.* **2020**, *220*, 111024. [CrossRef]
16. Zhao, H.; Tao, M.-X. Seismic behaviour of structural systems with separated gravity and lateral resisting systems. *J. Constr. Steel Res.* **2020**, *174*, 106315. [CrossRef]
17. Zhao, H.; Nie, X.; Zhu, D.; Tao, M.-X. Mechanical properties of novel out-of-plane steel beam–concrete wall pinned joints with T-shaped steel connectors under monotonic tension load. *Eng. Struct.* **2019**, *192*, 71–85. [CrossRef]
18. MSC Software Corp, *MSC.Marc*, version 2012; MSC Software: Newport Beach, CA, USA, 2012.
19. Genikomsou, A.S.; Polak, M.A. Finite element analysis of punching shear of concrete slabs using damaged plasticity model in ABAQUS. *Eng. Struct.* **2015**, *98*, 38–48. [CrossRef]
20. Wosatko, A.; Pamin, J.; Polak, M.A. Application of damage–plasticity models in finite element analysis of punching shear. *Comput. Struct.* **2015**, *151*, 73–85. [CrossRef]
21. Karalar, M. Experimental and numerical investigation on flexural and crack failure of reinforced concrete beams with bottom ash and fly ash. *Iran. J. Sci. Technol. Trans. Civ. Eng.* **2020**, *44*, 331–354. [CrossRef]
22. Karalar, M.; Bilir, T.; Çavuşlu, M.; Özkiliç, Y.O.; Sabri, M.M.S. Use of recycled coal bottom ash in reinforced concrete beams as replacement for aggregate. *Front. Mater.* **2022**, *9*, 1064604. [CrossRef]
23. Hognestad, E.; Hanson, N.W.; McHenry, D. Concrete Stress Distribution in Ultimate Strength Design. *J. Proc.* **1955**, *52*, 455–480. [CrossRef]
24. *Msc.MARC (2012) Volume A-Theory and User Information*; MSC.Software Corporation: Newport Beach, CA, USA, 2008.
25. Comité Euro-International du Béton-Fédération International de la Précontrainte (CEB-FIP). *CEB-FIP Model Code 2010: Design Code*; Thomas Telford: London, UK, 2010.
26. Rots, J.G.; Blaauwendraad, J. Crack models for concrete, discrete or smeared? Fixed, multi-directional or rotating? *HERON* **1989**, *34*, 1–59.
27. Bažant, Z.P.; Oh, B.H. Crack band theory for fracture of concrete. *Matér. Constr.* **1983**, *16*, 155–177. [CrossRef]

28. Wittmann, F.H.; Roelfstra, P.E.; Mihashi, H.; Huang, Y.-Y.; Zhang, X.-H.; Nomura, N. Influence of age of loading, water-cement ratio and rate of loading on fracture energy of concrete. *Mater. Struct.* **1987**, *20*, 103–110.

29. Wittmann, F.H.; Rokugo, K.; Brühwiler, E.; Mihashi, H.; Simonin, P. Fracture energy and strain softening of concrete as determined by means of compact tension specimens. *Mater. Struct.* **1988**, *21*, 21–32.

30. Wittmann, F.H. Crack formation and fracture energy of normal and high strength concrete. *Sadhana* **2002**, *27*, 413–423.

31. du Béton, C.E.-I. *CEB-FIP Model Code 1990: Design Code*; Thomas Telford Publishing: London, UK, 1993.

32. Nie, J.; Tao, M.; Cai, C.; Chen, G. Modeling and investigation of elasto-plastic behavior of steel–concrete composite frame systems. *J. Constr. Steel Res.* **2011**, *67*, 1973–1984. [CrossRef]

33. Hu, H.-S.; Nie, J.-G.; Wang, Y.-H. Effective stiffness of rectangular concrete filled steel tubular members. *J. Constr. Steel Res.* **2016**, *116*, 233–246. [CrossRef]

34. Guo, Y.-T.; Chen, J.; Nie, X.; Tao, M.-X.; Wang, J.-J.; Fan, J.-S. Investigation of the shear resistances of steel–concrete–steel composite structures with bidirectional webs. *J. Constr. Steel Res.* **2020**, *164*, 105846. [CrossRef]

35. *GB50010-2010*; Code for Design of Concrete Structures. China Architecture & Building Press: Beijing, China, 2010. (In Chinese)

36. Lu, X.; Ye, L.; Teng, J.; Jiang, J. Meso-scale finite element model for FRP sheets/plates bonded to concrete. *Eng. Struct.* **2005**, *27*, 564–575. [CrossRef]

37. Lu, X.; Jiang, J.; Teng, J.; Ye, L. Finite element simulation of debonding in FRP-to-concrete bonded joints. *Constr. Build. Mater.* **2006**, *20*, 412–424. [CrossRef]

38. Tao, M.-X.; Nie, J.-G. Multi-scale modeling for deformation mechanism analysis of composite joint substructures. *Eng. Struct.* **2016**, *118*, 55–73. [CrossRef]

39. Ollgaard, J.G.; Slutter, R.G.; Fisher, J.W. Shear strength of stud connectors in lightweight and normal-weight concrete. *AISC Eng. J.* **1971**, *8*, 55–64.

40. *GB 50017-2017*; Standard for Design of Steel Structures. China Architecture & Building Press: Beijing, China, 2017. (In Chinese)

41. *GB/T 10433-2002*; Cheese Head Studs for Arc Stud Welding. China Quality and Standards Publishing & Media Co.,Ltd.: Beijing, China, 2002. (In Chinese)